

# Development of Nanoscale Inhomogeneities during Drying of Sol–Gel Derived Amorphous Lead Zirconate Titanate Precursor Thin Films

Tomasz M. Stawski,<sup>†</sup> Sjoerd A. Veldhuis,<sup>†</sup> Hessel L. Castricum,<sup>‡</sup> Enrico G. Keim,<sup>†</sup> Guy Eeckhaut,<sup>§</sup> Wim Bras,<sup>||</sup> Dave H. A. Blank,<sup>†</sup> and Johan E. ten Elshof<sup>†,¶</sup>

<sup>†</sup>MESA<sup>+</sup> Institute for Nanotechnology, University of Twente, P. O. Box 217, 7500 AE Enschede, The Netherlands

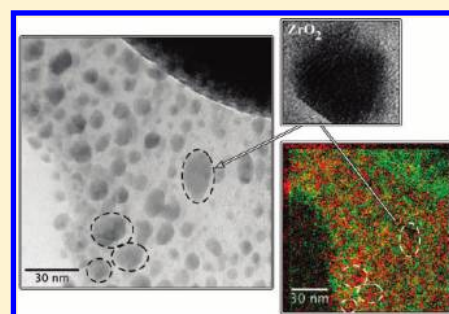
<sup>‡</sup>Van't Hoff Institute for Molecular Sciences, University of Amsterdam, Science Park 904, 1098 XH Amsterdam, The Netherlands

<sup>§</sup>Janssen Pharmaceutica, Turnhoutseweg 30, 2340 Beerse, Belgium

<sup>||</sup>Netherlands Organization for Scientific Research, DUBBLE@ESRF, BP 220, Grenoble F38043, France

**S** Supporting Information

**ABSTRACT:** The structural evolution of sol–gel derived lead zirconate titanate (PZT) precursor films during and after physical drying was investigated by transmission electron microscopy (TEM), electron energy loss spectroscopy (EELS), selected area electron diffraction (SAED), and time-resolved X-ray diffraction (XRD). Films were deposited from initial 0.3 mol/dm<sup>3</sup> precursor sols with varying hydrolysis ratios. Zr-rich grains of 1–10 nm size, embedded in a Pb-, Zr-, and Ti-containing amorphous matrix were found in as-dried films. The Zr-rich regions were crystalline at hydrolysis ratios [H<sub>2</sub>O]/[PZT] < 27.6, and amorphous at ratios > 100. X-ray diffraction analysis of PZT and zirconia sols revealed that the crystalline nanoparticles in both sols are identical and are probably composed of nanosized zirconium oxoacetate-like clusters. This study demonstrates that time-resolved X-ray diffraction combined with electron energy loss spectroscopy mapping is a powerful tool to monitor the nanoscale structural evolution of sol–gel derived thin films.



## 1. INTRODUCTION

Because of its wide range of applications, a lot of interest has been dedicated to the fabrication and characterization of lead zirconate titanate (PbZr<sub>1-x</sub>Ti<sub>x</sub>O<sub>3</sub>; PZT) thin films.<sup>1–4</sup> PZT is technologically important because of its large remnant polarization, low coercive field, and high piezoelectric coefficients. There are two major routes for the fabrication of thin films, namely, via physical and wet-chemical techniques. The physical techniques include metal–organic chemical vapor deposition (MOCVD),<sup>5,6</sup> sputtering,<sup>7,8</sup> and pulsed laser deposition.<sup>9,10</sup> The chemical solution deposition (CSD) techniques<sup>11</sup> include the sol–gel route,<sup>12,13</sup> metal–organic deposition (MOD),<sup>14,15</sup> and chelate synthesis.<sup>12</sup> Among the latter, the sol–gel technique has attracted considerable attention because of its simplicity, low cost, good compositional control, and its ability for large-area film fabrication.<sup>16</sup>

Typical sol–gel solutions consist of metal alkoxides and/or metal carboxylate precursors, solvents, water, and catalyst. They can be deposited as thin films by dip-coating or spin-coating, after which they get a thermal treatment at high temperature for consolidation and PZT phase formation. It is known that the nature of the sol has a profound effect on the microstructure, orientation, and electrical properties of the final films.<sup>12,16</sup> The structural chemistry of PZT sols has been studied by various analytical techniques, such as nuclear magnetic resonance (NMR),<sup>17–21</sup>

Fourier transform infrared (FTIR),<sup>19,20</sup> gas chromatography–mass spectroscopy (GC-MS),<sup>18</sup> photon correlation spectroscopy (PCS),<sup>21–23</sup> and small-angle X-ray scattering (SAXS).<sup>21–23</sup> It has been noted, e.g., in the reviews of Schwartz et al.,<sup>11,24,25</sup> that hardly any information is available about the structural evolution of PZT sols in later stages of the sol–gel process, such as during and after the drying of as-deposited thin films.

The properties of sols are controlled by the nature of the metal-carrying reagent, solvent, reagent concentration, water concentration, method of water addition, catalyst, solution preparation/reaction conditions, and other factors.<sup>11,12,24,25</sup> For multicomponent (mixed metal) systems such as PZT, prehydrolysis of less reactive metal alkoxides is sometimes employed to improve compositional uniformity. Earlier studies showed that soluble oligomers instead of precipitates can only be formed under water-lean conditions.<sup>25</sup> A key point is therefore to restrict the amount of water and to control the way in which it is added. Assink and Schwartz reported that acetic acid acts as a key chelating agent, affecting the reactivity and promoting esterification reactions that result in many alkyl acetate esters as byproducts. This

**Received:** May 20, 2011

**Revised:** July 6, 2011

**Published:** July 07, 2011

suggests the formation of metal acetates and/or metal alkoxy acetates due to (partial) exchange of alkoxy ligands by acetate,<sup>17</sup> but detailed knowledge of the nature of precursor species in PZT solutions after water addition (hydrolysis) is scarce. An extended X-ray absorption fine structure (EXAFS) study of commonly used nonhydrolyzed PZT sols showed that the constituent solvent/modifiers such as acetic acid and acetylacetone have an effect on the degree of homogeneity in the distribution of Pb and Zr, but Pb–O–Zr bonds could not be determined in any of the samples.<sup>26</sup> It is believed that most metal alkoxides and metal carboxylates can form oligomeric structures in appropriate solvents. Well-known examples are  $\text{Ti}_6(\text{O}^i\text{Pr})_{10}(\text{OOCCH}_3)_4\text{O}_4$ ,  $\text{Ti}_6(\text{O}^i\text{Pr})_8(\text{OOCCH}_3)_8\text{O}_4$ , and  $\text{Zr}_4\text{O}(\text{OPr})_{10}(\text{CH}_3\text{COCH}_2\text{-COCH}_3)$ .<sup>11,12</sup> Complexes of Pb and Ti or Zr precursors in similar solvents have also been reported, e.g.,  $\text{PbTi}_2[(\mu_4\text{-O})\text{-}(\text{OOCCH}_3)(\text{OCH}_2\text{CH}_3)_7]_2$ ,  $\text{Pb}_4\text{Zr}_4(\mu\text{-O}_2\text{CR}')_8(\text{O}^i\text{Pr})_{16}\text{-}(\text{OH}^i\text{Pr})_2$ ,  $\text{Pb}_2\text{Ti}_4(\mu\text{-O}_2\text{CR}')_4(\text{OR})_{16}$ ,  $\text{Pb}_2\text{Ti}_3(\mu_4\text{-O})(\mu_3\text{-O})\text{-}(\mu\text{-O}_2\text{CC}_7\text{H}_{15})_2(\mu\text{-O}^i\text{Pr})_6(\text{O}^i\text{Pr})_4$ ,  $\text{PbZr}_3(\mu_4\text{-O})(\text{OAc})_2(\text{O}^i\text{Pr})_{10}$ , and several others.<sup>27–31</sup> All these complexes formed in the absence of water, i.e., without the hydrolysis step (water addition) that is typical for initiating sol–gel processes.

In the drying stage of sol–gel films the situation becomes even more complex, as complexation reactions and evaporation occur simultaneously, and there is a mutual influence.<sup>24,25,32</sup> For instance, loss of solvent due to physical drying increases the solution viscosity and reaction rate of species that are present in that solution. If more than one solvent is used, differences in the relative solvent evaporation rates at a given temperature lead to a gradually changing matrix for the sol particles, which may affect their solubility and reactivity, and induce phase separation. Moreover, in comparison with many polar organic solvents, water is a relatively volatile reagent that may be evaporated before it is consumed in a thin film drying process. Obviously, this may have an effect on the final structure of the as-dried thin film. Neutron scattering studies indicated that alkoxide-based PZT sol–gel processing results in compositionally inhomogeneous samples.<sup>33</sup> This is due to compositional segregation that appears to occur early on during sol–gel processing and is not fully eliminated by the final high-temperature heat treatment.

It is the aim of this study to elucidate structural aspects of sol–gel PZT precursor thin films in the course of and directly after the drying process, in which volatile components are lost from the film, and precursor concentrations increase progressively. We used transmission electron microscopy (TEM), selected area electron diffraction (SAED), and electron energy loss spectroscopy (EELS) for the characterization of as-deposited dried precursor films. Time-resolved SAXS and diffraction experiments at small angles were used to monitor the structure and structural evolution of PZT sols and drying thin films on nanometer length scale. In particular, we focused on a commonly used PZT solution composition that has been used by us to imprint PZT nanopatterns with a lateral resolution below 200 nm by soft lithography<sup>34</sup> and is based on the combination of acetic acid and 2-methoxyethanol as solvents.<sup>11–13,21–26</sup> We investigated a selected number of solutions and process conditions, to get insight into the structures that formed in the sol stage, and into the processes that occurred in situ on the nanoscale when a PZT sol–gel thin film was being dried.

## 2. EXPERIMENTAL SECTION

**Synthesis of Lead Zirconate Titanate Precursor Sols.** Lead-(II) acetate trihydrate (99%, Sigma-Aldrich), zirconium(IV) *n*-propoxide

(70% (w/w) in *n*-propanol, Alfa Aesar), and titanium(IV) isopropoxide (99.999%, Sigma-Aldrich) were used as precursor materials. Glacial acetic acid (99.8%, Acros) and 2-methoxyethanol (>99.3%, Sigma-Aldrich) were used as solvents, stabilizers, and chelating agents. Initially, three stock solutions were made. A lead acetate solution was prepared by dissolving lead acetate trihydrate in acetic acid and subsequent refluxing at 105 °C for 8 h to remove all remaining water.<sup>13</sup> The other two solutions, based on titanium isopropoxide and zirconium *n*-propoxide, respectively, were dissolved in 2-methoxyethanol and stirred in a glovebox under nitrogen atmosphere. All stock solutions were stirred at room temperature for 24 h. They were then stored at room temperature. The concentration of individual stock solutions was 0.60 mol/dm<sup>3</sup>. Prior to experiments, the stock solutions were mixed in the appropriate molar ratios and stirred for 5–10 min. Normally, Ti and Zr stock solution had been mixed first and added to lead acetate solution in acetic acid. The molar ratio of Pb to Zr to Ti was always kept at 100:52:48, yielding a concentration of 0.30 mol/dm<sup>3</sup> in the final PZT solution. Solutions of this concentration constituted the basis for all experiments. In the case of hydrolyzed solutions, water was immediately added after the three stock solutions had been mixed. The hydrolysis ratio (*h*) of the PZT sols is defined as

$$h = \frac{[\text{H}_2\text{O}]}{[\text{PZT}]} \quad (1)$$

where  $[\text{H}_2\text{O}]$  and  $[\text{PZT}]$  are the concentrations of H<sub>2</sub>O and PZT precursors in solution, respectively. PZT sols with *h* = 0.0, 2.3, 4.6, 9.3, 27.6, 55.5, and 111 were investigated. It is noted that the value of *h* is a nominal value that does not include traces of water that may result from a natural esterification reaction of the solvents, i.e.,  $\text{H}_3\text{CCOOH} + \text{HO-C}_2\text{H}_4\text{-OCH}_3 = \text{H}_3\text{CCOO-C}_2\text{H}_4\text{-OCH}_3 + \text{H}_2\text{O}$ .

**Synthesis of Zirconia Precursor Sol.** Zirconium(IV) *n*-propoxide (70% (w/w) in *n*-propanol, Alfa Aesar) was used as a precursor material. Glacial acetic acid (99.8%, Merck) and 2-methoxyethanol (99.3%, Sigma-Aldrich) were used as chelating agents, solvents, and stabilizers. A zirconium(IV) *n*-propoxide solution was dissolved in 2-methoxyethanol and stirred in a glovebox under nitrogen atmosphere, yielding a 1.00 mol/dm<sup>3</sup> stock solution of zirconium(IV) methoxyethoxide. In the next step, the zirconium(IV) methoxyethoxide stock solution was mixed with acetic acid yielding a 0.50 mol/dm<sup>3</sup> solution. Finally, the solution was hydrolyzed at *h* = 4.8.

**TEM, SAED, and EELS Characterization.** PZT precursor sols with *h* = 0, 9.3, 27.6, and 111, respectively, were spin-cast (Laurell WS-400B-6NPP-Lite spincoater) onto holey carbon TEM copper grids (CF200-Cu, Electron Microscopy Sciences) at 4000 rpm for 40 s. Then the as-prepared films were dried at 60 °C for 1 h on a hot-stage and used for transmission electron microscopy characterization (Philips CM300ST-FEG at 300 kV).

Samples were investigated at low magnification to find typical areas and features of interest were examined at high magnification (GATAN 2048 × 2048 Ultrascan1000 CCD camera). Crystallographic information was obtained by local Fourier transforms (FT) of areas of the images exhibiting high levels of crystallinity. The microscope software packages GATAN Microscopy Suite 1.8 and ImageJ 1.38e<sup>35</sup> were used for this purpose. Energy filtered images (GATAN model Tridium with 2048 × 2048 CCD camera) were recorded at the highest possible magnification that still provided stable images, with negligible or compensable drift using three-windows method for Zr–M<sub>4,5</sub> (preedge, 145 eV; postedge, 200 eV; slit width, 20 eV; 8 s exposure), Ti–L<sub>2,3</sub> (preedge, 406 eV; postedge, 481 eV; slit width, 30 eV; 10 s exposure), and Pb–M<sub>4,5</sub> (preedge, 2324 eV; postedge, 2534 eV; slit width, 100 eV; 40 s exposure). The mapping of Pb–M<sub>4,5</sub> using EELS is particularly tedious. It was established that the Pb distributions that we measured present significant mappings, as discussed in more detail in the Supporting Information. Due to the relatively long counting times necessary for Pb, some image drift occurred in

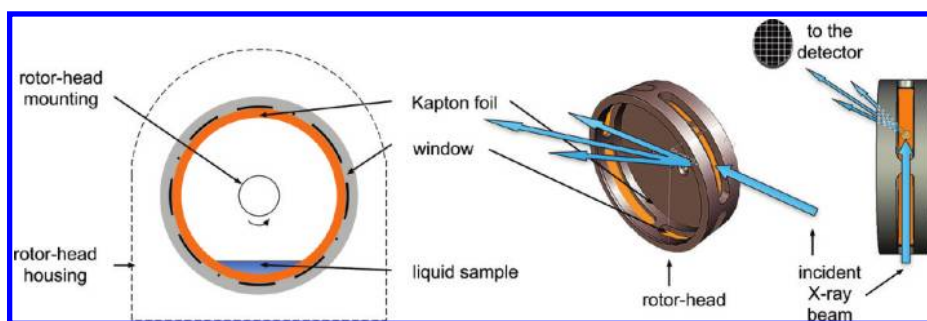


**Figure 1.** Schematic of the setup used for in situ X-ray scattering measurements of drying PZT precursor films.

some cases. Color-mix maps juxtapositioning selected combinations of elements were manually corrected for drift depending on the element, using the microscope GMS software package. Electron diffraction images were taken at effective camera lengths of 587 and 774 nm (collected with Ultrascan1000 CCD camera).

**Time-Resolved X-ray Diffraction during Drying of PZT Films and Precipitation of PZT Sols.** Time-resolved X-ray diffraction and small-angle X-ray scattering experiments were performed on the Dutch-Belgian beamline (DUBBLE) BM-26B of the ESRF in Grenoble, France.<sup>36</sup> We used a dedicated small-angle X-ray scattering beamline, due to the large lattice constants of the species found in our experiments. The beamline was suitable for measuring diffraction patterns at small angles. For some of the investigated sols we also measured typical small-angle scattering (SAXS) curves. In SAXS experiment, the elastic scattering of X-rays by a sample that has local electronic density fluctuations was recorded at small angles. Structural information with dimensions of 0.25–50 nm can be derived from this angular range.<sup>37,38</sup> The scattering intensity  $I(q)$  is recorded versus the scattering vector  $q$  ( $\text{nm}^{-1}$ ), which is related to the scattering angle  $\theta$  and the wavelength  $\lambda$  (nm) of the incident beam via

$$q = \frac{4\pi}{\lambda} \sin \theta \quad (2)$$

The beam energy was 16 keV ( $\lambda = 0.0776$  nm). The beam was focused at the corner of a 2D gas-filled multiwire proportional CCD detector in order to maximize the range of accessible  $q$  (scattering vector) values. The samples were placed at a distance of 1.5 m from the detector, and the intensity was measured in the scattering vector range  $0.13 < q < 8.2$   $\text{nm}^{-1}$ . The raw data were corrected for the pixel-dependent detector sensitivity. By applying eq 2 and Bragg's law for diffraction

$$\lambda = 2d \sin \theta \quad (3)$$

where  $d$  is the lattice plane spacing in real space, the above-mentioned scattering vector range is equivalent to the plane spacing range  $48.3 < d < 0.76$  nm for crystalline materials.

To study the structure of PZT precursor sols, small quantities of solutions were contained in a sealed borosilicate glass capillary (i.d. = 1.5 mm, glass no. 14, Hilgenberg, Malsfeld, Germany) and measured at room temperature. PZT sols with  $h = 0.0, 2.3, 4.6, 9.3, 27.6, 55.5$ , and 111 after aging for 40 h at 60 °C in sealed containers were used in these studies. The scattering intensity from a capillary containing only the corresponding solvent(s) was subtracted from the overall intensity signal, whereby a correction was made for the fact that the concentration of solvent in a sol is lower than in the pure solvent. The scattering and diffraction data were collected for periods of typically 2–5 min at room temperature. To investigate the growth or precipitation of zirconia sols at elevated temperatures, scattering curves  $I(q) - q$  were collected on sols in borosilicate glass sealed capillaries (i.d. = 1.0 mm, glass no. 14, Hilgenberg, Malsfeld, Germany) that were mounted into a programmable thermostat (Linkam) that was heated to 60 °C. Measurements were

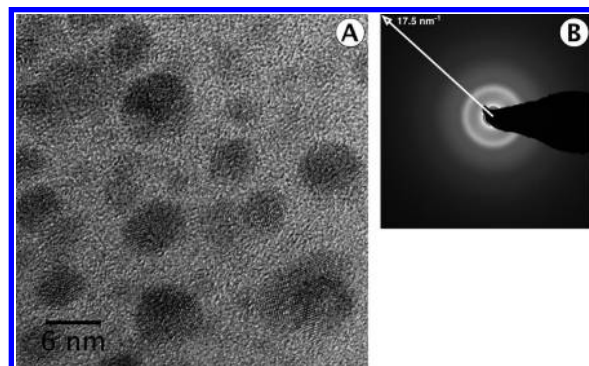


**Figure 2.** (A) TEM bright-field images of dried films from fresh PZT precursor sols with  $h = 0$ . (B) Representative electron diffraction pattern of film from fresh sol without added water at  $L = 587$  nm.

done with 2–5 min intervals for time periods of typically 1 h. Time-resolved scattering patterns of a developing zirconia precursor sol ( $h = 4.8$ ) were recorded for 60 min at 60 °C in a capillary using a Linkam heating stage.

The setup that was used to follow the evolution of drying thin films is schematically illustrated in Figure 1. PZT sols were contained in a Kapton foil that was mounted on an aluminum rotor head with a diameter of ca. 11 cm. The rotation speed was 100 rpm, ensuring a homogeneous distribution of liquid film over the surface of the Kapton foil. The rotation axis was not completely perpendicular to the incoming X-ray beam, as illustrated in Figure 1. This allowed detection of the scattered or diffracted X-ray beam. The scattering intensity was recorded at 60 °C at regular time intervals for 40 min. The scattering intensity of the empty chamber, i.e., Kapton foil under the same conditions, was subtracted as correction for the background contribution. Time-resolved SAXS patterns of drying PZT thin films with  $h = 9.3$  were recorded at 60 °C for 40 min using this setup.

### 3. RESULTS AND DISCUSSION

**TEM and EELS Analysis of As-Dried PZT Thin Films.** The dried films prepared from fresh solutions of PZT sols with  $h = 0.00, 9.3$ , and 27.6 exhibited practically the same microstructure. See Figure 2A,B and 3A. In all three samples the film consisted of an amorphous matrix with numerous embedded highly crystalline particles with a diameter of 1–10 nm. The amorphous structure of the matrix was confirmed by the representative SAED pattern of Figure 2B.

Figure 3A shows an area from the film from a PZT sol with  $h = 27.6$ . The area contains highly crystalline particles. The corresponding Fourier transforms of three selected particles are

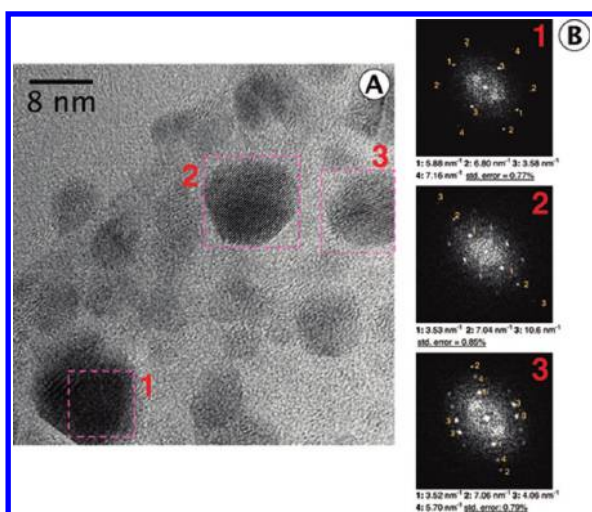


**Figure 3.** (A) TEM bright-field image of an area from the film made from fresh PZT precursor sol with  $h = 27.6$ . (B) FT images of the selected areas 1, 2, and 3 including corresponding crystallographic data.

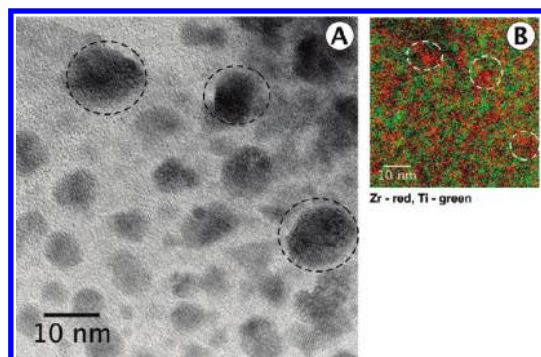


**Figure 4.** (A) TEM bright-field image of the film made from fresh PZT precursor sol with  $h = 27.6$ . (B) Corresponding elemental EELS mappings of Zr and Ti, combined into color image.

shown in Figure 3B. The quality of the FTs depends on the quality and size of the crystalline region of interest. Minimal drift or a different focus plane can lead to an asymmetric shape of the peak in reciprocal space and make analysis difficult. The accuracy also decreases with increasing length of  $1/d$ . The data revealed spots at characteristic values of  $1/d$  at approximately 3.60, 4.06, 5.88, 6.80, 7.16, and  $10.1 \text{ nm}^{-1}$ . The same characteristic lengths were found in films from sols with  $h = 0$  and 9.3 (not shown here). Only small differences were found between different FTs.

The local composition of the films was investigated by a derivative mode of energy-filtered TEM (EF-TEM) termed electron energy loss spectroscopy. EELS analysis yielded two-dimensional qualitative maps of the distribution of specific elements in a film. The highest possible magnifications that still provided negligible or compensable image drift were applied.

Figure 4A shows an unfiltered TEM image of an as-dried film, made from a PZT sol with  $h = 27.6$ . Some crystalline areas are indicated by circles. The near-corresponding combined EELS maps with the distributions of Zr and Ti are shown in Figure 4B. The indicated crystalline particles from Figure 4A correspond with areas of high Zr and low Ti concentration. The spatial position between regions of interest in Figure 4A,B is not exactly the same (the same refers to other elemental maps), as the

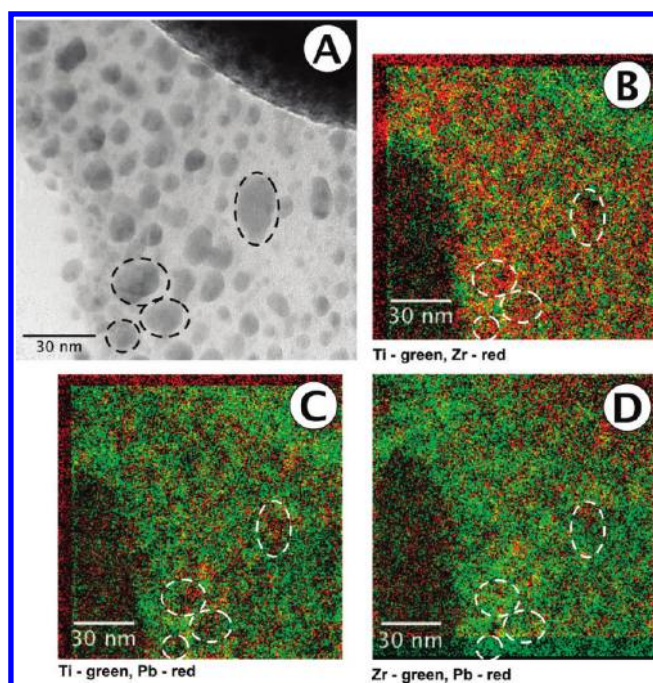


**Figure 5.** (A) TEM bright-field image of the film made from the fresh PZT precursor sol without water, i.e.,  $h = 0.00$ . (B–D) Corresponding combined elemental EELS mappings of (B) Ti and Zr, (C) Ti and Pb, and (D) Zr and Pb.

position of the nanoparticles embedded in the matrix can be slightly influenced by the electron beam.

Similar element distribution maps of Ti, Zr, and Pb were also made of a film deposited from a water-free PZT sol ( $h = 0$ ). Figure 5A shows the unfiltered TEM image, again containing dark crystalline nanoparticles. When the Ti and Zr distribution maps are superimposed in Figure 5B, the same Zr enrichment in crystalline areas can be seen. Figure 5C shows the distributions of Pb and Ti. Ti is detected primarily in the amorphous areas of the film, while Pb seems to be distributed homogeneously over the entire area. But the crystalline areas are more strongly enriched in Zr than that they contain Pb (Figure 5D). However, Zr is also present in the amorphous matrix. It may be concluded that the crystalline nanoparticles in all investigated films contain primarily Zr. The amorphous matrix, in which the particles are embedded, contains Ti, Zr, and Pb.

The high Zr concentration in the crystalline nanograins of Figures 2–5 suggests that it is a zirconium oxide-related phase. The  $1/d$ -values of the FTs and their relative intensities agree with diffraction data from various phases  $\text{ZrO}_x$ , especially some of the recently characterized phases of zirconia nanopowders derived from wet-chemical synthesis routes.<sup>39,40</sup> More accurate identification is not possible due to the limited number of diffraction peaks, the polymorphism of zirconium oxide, and the limited size of the nanograins. However, in view of the environment in which these nanograins developed, it is very unlikely that a substoichiometric zirconia phase would have developed, so on the basis of all available experimental data, it is plausible that the nanograins consist of  $\text{ZrO}_2$ .

An experiment with a large excess of water,  $h = 111$ , was carried out to determine its influence on the morphology of as-deposited films. In this experiment water rather than organic solvents was the main component of the solvent mixture. A bright-field TEM

image of the corresponding as-deposited film is shown in Figure 6A. Darker grainlike regions, similar in size and shape to the ones shown in Figures 2–5, can be seen, but in this case the grains were virtually amorphous instead of crystalline. Parts B and C of Figure 6 show the bright-field TEM and corresponding EELS mappings of Zr and Ti, respectively, in more representative regions. Figure 6C shows that the dark regions in Figure 6B

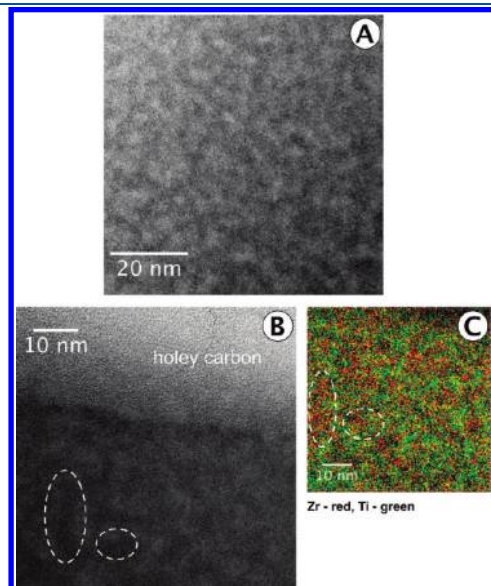


**Figure 6.** (A) TEM bright-field image of film made from fresh PZT precursor sol with  $h = 111$ . (B) Bright-field TEM image of the same film recorded in a different area of the TEM specimen. (C) Corresponding elemental EELS mappings of Zr and Ti, combined into color image.

correspond to areas with increased Zr concentration. Areas with majority concentrations of Zr and Ti are separated from each other on a length scale less than 10 nm. These results demonstrate that the crystalline character of the Zr-rich nanoparticles shown in Figures 2–5 is somehow related to the lower hydrolysis ratios in those sols. So while Zr-rich areas are still being formed at high water concentrations, their morphology is different, giving less or no evidence for crystallinity.

Aging of PZT sols has a significant effect on the microstructure of the as-dried films. Films prepared from sols ( $h = 0$ ) that had been aged for 40 h exhibited another microstructure than the films made from fresh sols. Figure 7A also shows evidence of agglomerate-like structures of  $\sim 40$  nm diameter in the film. The corresponding EELS mappings in Figure 7B–D show a particle-like structure near the bottom of the figure, indicated by a dotted circle, that is strongly enriched in Zr and is surrounded by an area that is strongly enriched in both Pb and Ti. A global SAED pattern of a film from an aged sol is shown in Figure 7E. Peak positions in the  $1/d$  representation were found at approximately 3.65, 4.10, 4.97, 5.88, 6.70, 8.23, 8.95, and  $10.1 \text{ nm}^{-1}$ . Comparison of these values with the FTs in Figure 3B leads to the conclusion that the crystal structure in the polycrystalline film of Figure 7 closely resembles the structure of the  $\text{ZrO}_2$  nanoparticles in Figures 2–5. Small differences between the reciprocal distances, of the order of 2% or less, can be explained by differences in the calibrations of the camera length in SAED and HR-magnification in TEM.

**Time-Resolved XRD on Drying Thin Films.** To determine the structure of PZT sols in stages prior to the dried film stage, X-ray scattering/diffraction experiments were carried on 40 h aged PZT sols and in situ on drying thin films. This allowed us to investigate and explain the emergence of the structural and

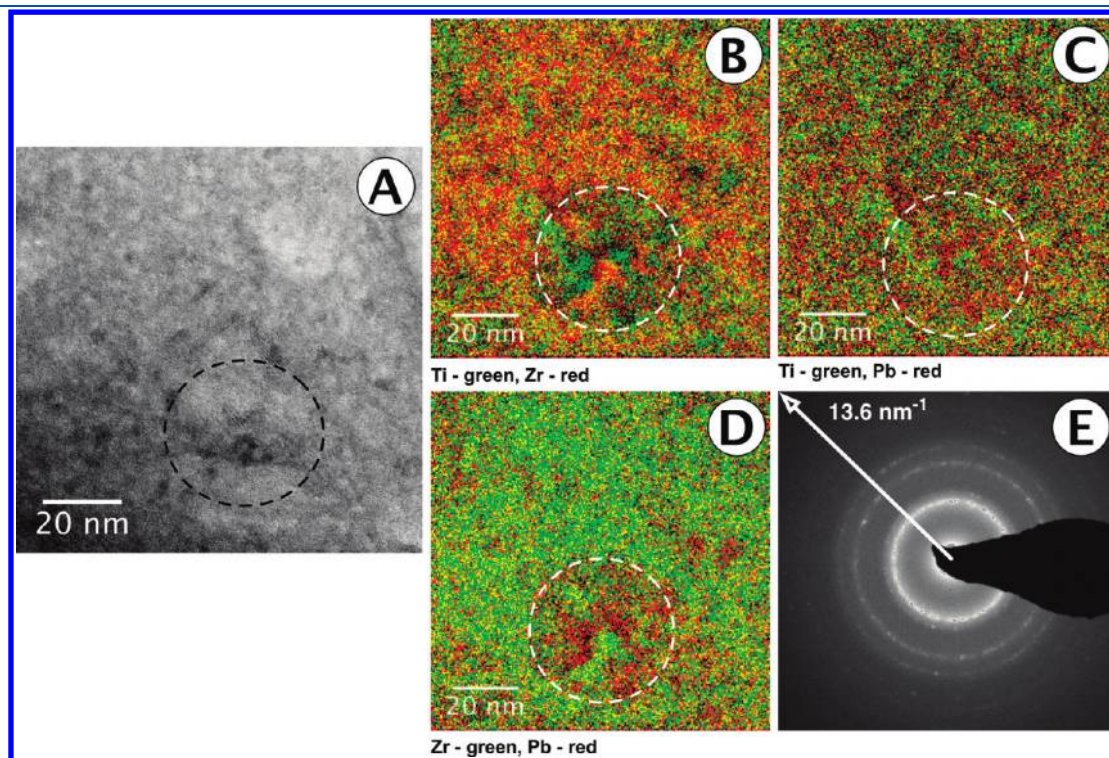


**Figure 7.** (A) TEM image of film made from aged PZT precursor sol ( $h = 0.0$ ). EELS mappings of (B) Zr and Ti, (C) Pb and Ti, (D) Pb and Zr, and (E) SAED pattern of film from aged PZT sol ( $h = 0$ ).

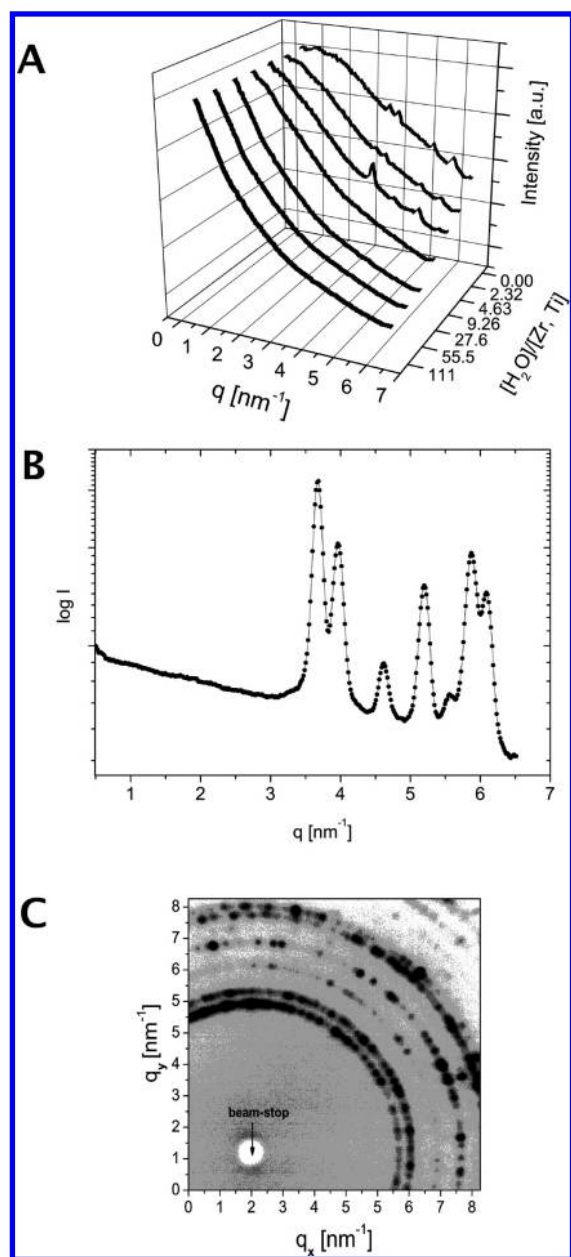


**Figure 8.** (A) SAXS patterns of  $0.3 \text{ mol/dm}^3$  PZT precursor sols with  $[\text{H}_2\text{O}]/[\text{Ti} + \text{Zr}]$  between 0 and 111. (B) SAXS/diffraction pattern of the phase precipitated from the PZT sol with  $[\text{H}_2\text{O}]/[\text{Ti} + \text{Zr}] = 0.00$ . (C) 2D SAXS/diffraction pattern of the same sol.

compositional phenomena observed in as-dried films, as was discussed in the preceding section. Scattering/diffraction patterns of aged PZT precursor sols with varying  $h$  are shown in Figure 8A. In aged sols with  $h$  between 0.00 and 4.6, characteristic Bragg peaks developed. The narrow full width at half-maximum (fwhm) of these peaks indicates a high degree of order, which resulted from a crystallization process that occurred in the solution during aging. Sols with  $h > 9$  did not exhibit any sign of precipitation even after 40 h of aging at  $60^\circ\text{C}$ . In contrast, a precipitate could already be collected from the PZT sol without added water after a few minutes of aging.

The diffraction pattern of the precipitate is shown in Figure 8B,C. The Bragg peaks are located at scattering vector positions  $q = 3.69, 3.97, 4.62, 5.20, 5.56, 5.87, \text{ and } 6.09 \text{ nm}^{-1}$ , which

corresponds to  $1/d$ -values of  $0.587, 0.632, 0.735, 0.828, 0.885, 0.934, \text{ and } 0.969 \text{ nm}^{-1}$ , respectively. The single spots in the 2D diffraction pattern in Figure 8C are indicative of a system with a small number of relatively large grains. Precipitates contained in sols with  $h$  up to 4.6 exhibited similar though less pronounced patterns.

As was shown in the TEM analysis, the crystalline nanograins present in the as-dried PZT films and the precipitate from aged solutions contained mostly or exclusively Zr. By performing a series of simple mixing reactions of pairs of the three stock solutions and the two solvents (acetic acid and 2-methoxyethanol), it was found that precipitation was probably caused by the reaction between zirconium alkoxide and acetic acid. It is most likely that an oligomeric zirconium alkoxyacetate or oxoacetate phase formed when  $h$  was small. Figure 9A illustrates the stability of a  $0.50 \text{ mol/dm}^3$  solution of zirconium(IV) methoxyethoxide in acetic acid at  $60^\circ\text{C}$ . Bragg peaks of a precipitating crystalline phase were detected after 28 min of reaction. The corresponding 2D scattering pattern after 60 min is shown in Figure 9B. It demonstrates that the evolving Bragg peaks in Figure 9A result from a small number of crystalline grains. The peaks of the isotropic one-dimensional scattering pattern are at scattering vector positions  $q = 3.69, 3.99, 4.63, 5.21, 5.62, 5.90, \text{ and } 6.11 \text{ nm}^{-1}$ . These  $q$ -values are in excellent agreement with those of the precipitates in the PZT precursor sols as shown in Figure 8. This suggests strongly that the precipitating phase in the PZT precursor sol is predominantly or exclusively related to the Zr component. Differences in relative intensities of corresponding peaks can be explained in terms of preferred orientation of crystals, as illustrated by the single reflections that are visible as isolated spots in Figure 9B. It is apparent that the precipitating phase from PZT precursor sols contain the same or very closely related crystalline phase as the precipitate from a pure zirconia precursor sol when  $h < 5$ . In contrast, PZT sols with  $h > 9$  did not show any evolving crystalline phase for at least 40 h at  $60^\circ\text{C}$ . From the peak positions we attempted to identify the phase from Figures 8 and 9. The high values of  $d$  indicated the presence of an organometallic Zr compound in the group of zirconium alkoxy-carboxylates. Such crystals usually contain clusters composed of a hexanuclear octahedral zirconium oxo-hydroxo core and surrounding alkoxy and carboxy ligands, e.g.,  $[\text{Zr}_6(\mu_3\text{-O})_4(\mu_3\text{-OH})_4(\text{OOCR})_{12}]$ , where R = *tert*-butanoate, 2-methylpropanoate, propanoate, or acetate.<sup>41–43</sup> The actual crystal structure depends on the ligand environment. Furthermore, depending on the nature of the carboxylic acid group, dimerized hexanuclear clusters of general formula  $[\text{Zr}_6\text{O}_4(\text{OH})_4(\text{OOCR})_{12}]_2$  have been synthesized, in which two hexanuclear subunits are bridged by four carboxylate ligands.<sup>43</sup> These clusters have the same stoichiometry but cannot be easily converted from one into the other despite their structural similarity. These systems obviously yield different diffraction patterns. In our experiments we used zirconium(IV) methoxyethoxide and an excess of acetic acid. *n*-Propanol and water molecules were also available in the sol. To the best of our knowledge, the crystal structure of a compound prepared under exactly the same conditions has never been solved and published. Nevertheless, on the basis of X-ray diffraction pattern simulations from structural data of  $[\text{Zr}_6\text{O}_4(\text{OH})_4(\text{OOCR})_{12}]_2$  complexes, we found close similarity between these hexanuclear octahedral zirconium oxo dimers and the compound in our experiments. Therefore, we refer to this crystalline nanophase as zirconium oxoacetate clusters.

Thin film drying experiments using these sols were carried out with the designed setup (Figure 1). A small volume of liquid was

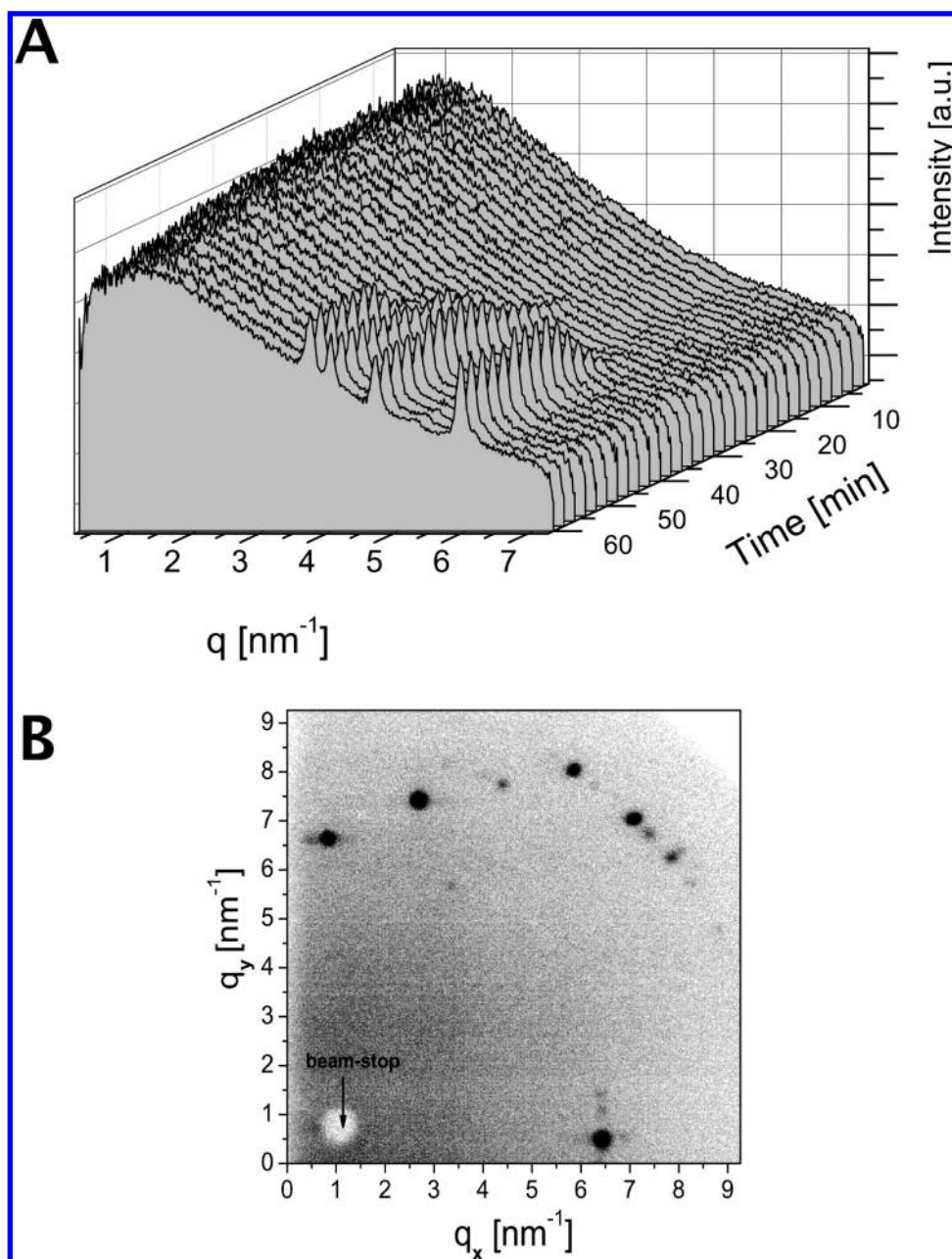


**Figure 9.** (A) Time-resolved X-ray scattering patterns of developing  $0.50 \text{ mol/dm}^3$  zirconia precursor sol at  $60^\circ \text{C}$ . (B) 2D SAXS pattern of zirconia precursor sol after 60 min of reaction.

dropped into the rotating cylinder, just sufficient to form a thin wet PZT film that covered the entire spinning Kapton film, and dried in air. Figure 10 show the time-resolved SAXS patterns of a drying film from a stable PZT precursor sol with  $h = 9.3$  at  $60^\circ \text{C}$ . A crystalline phase developed soon after drying started. The first indications appeared after about 4 min. The PZT film was most likely dry after 10–12 min, when the scattering intensity reached a plateau. By this time the scattering intensity had decreased by  $\sim 90\%$  or more over the entire  $q$ -range. This is an effect of solvent evaporation, which leads to loss of scattering contrast. The solid precursor entities in the film approach each other and agglomerate into larger structures in the course of drying. This leads to increasingly homogeneous film morphology, with accompanying loss of scattering contrast between scatterers and

their surroundings. Furthermore, heavier elements such as Ti and especially Zr and Pb absorb light, which leads to a decrease in scattering intensity. A detailed view into the process between 14 and 20 min is presented in Figure 10B. A very strong peak with a maximum at  $q = 5.63 \text{ nm}^{-1}$ , accompanied by a weaker peak at  $q = 5.82 \text{ nm}^{-1}$ , can be recognized. Peaks are also present at  $q = 3.00$ ,  $3.69$ , and  $6.10 \text{ nm}^{-1}$ . The peaks at  $q = 5.6\text{--}6.1$  and  $3.69 \text{ nm}^{-1}$  can be attributed to the zirconium oxoacetate nanoparticles. The origin of peak at  $q = 3.00 \text{ nm}^{-1}$  is not exactly known, but it is probably related to another process taking place in the solution, possibly the aggregation of similarly sized nanoparticles.

#### Influence of Water and Acetic Acid on Structure of Films.

The data presented above are the result of nucleation from nanoscale inhomogeneities in the sol–gel solution.<sup>33,44</sup> Chemical

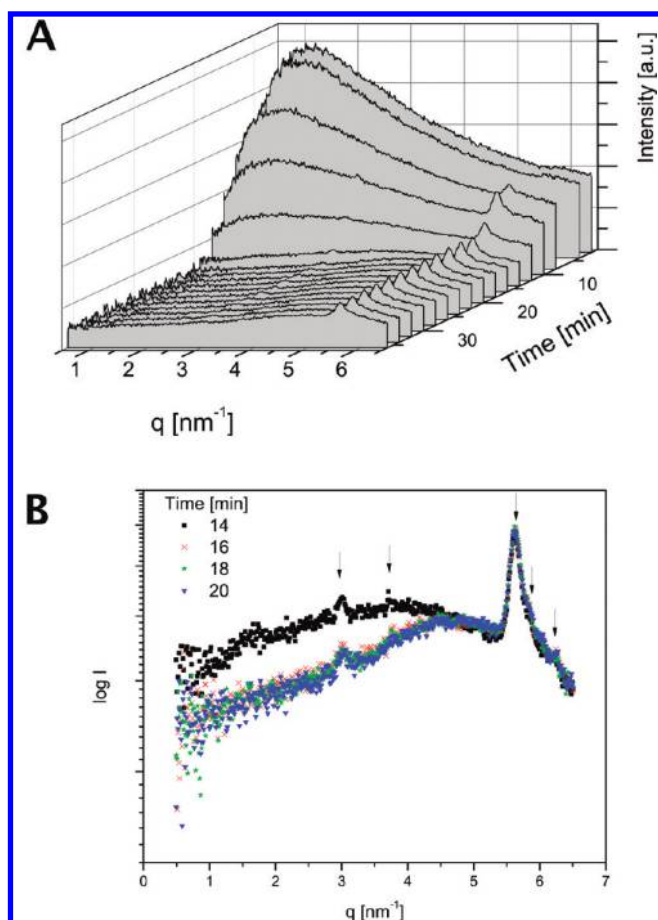


**Figure 10.** (A) Time-resolved X-ray scattering measurement of developing PZT precursor with  $h = 9.3$  upon drying at  $80\text{ }^{\circ}\text{C}$ . (B) Detailed view of the process between 14th and 20th minute.

heterogeneity has also been observed in neutron scattering studies on PZT powders.<sup>33</sup> It was found that the Zr/Ti ratio varied widely at different locations in the samples. EXAFS studies of partially heat-treated PZT made from a 2-methoxyethanol-based recipe also indicated chemical heterogeneity on an atomic level.<sup>45</sup> EXAFS on similar powders derived from metal *n*-butoxides indicated predominant Zr–O–Zr linkages, although Pb–O–Zr linkages were also observed.<sup>44</sup> Our observations are in agreement with these studies. Water is responsible for hydrolysis of the metal alkoxides and, hence, indirectly for the formation of sol particles. Second, due to its high polarity it facilitates dissociation in the solution. It should be noted that other polar solvents can play a similar role; e.g., methanol is often used in the inverted mixing order method for the PZT precursor sol–gel system.<sup>11,12,17,24</sup> The presence of ions prevents oligomeric species from agglomeration and precipitation. But even in a stable sol, nucleation of precipitates can still be induced once a film is being formed, and water and other solvents evaporate from it. No clear differences were found between the microstructures of dried PZT films that had been prepared with hydrolysis ratios anywhere between 0 and 27.6. This may be related to the presence of traces of water in the sample with nominal value  $h = 0$ . The crystalline particles are mainly Zr-based and most likely composed of zirconia. The amorphous matrix surrounding the Zr-rich grains contains both Zr and Ti, while Pb seems to be evenly distributed over the entire volume of the matrix. Even at the very high value  $h = 111$ , Zr-rich

regions were present, but they were amorphous instead of crystalline. This supports the hypothesis that, due to the high concentration of water in the drying film, it was present longer, thereby hindering crystallization of Zr-rich nanoparticles, or aiding in the transformation to an amorphous phase, e.g., a zirconium hydroxide related phase.

Acetic acid has been commonly used as stabilizing and chelating agent for many titanium and zirconium alkoxides.<sup>11–13,16–18,46</sup> The overall  $[\text{CH}_3\text{COOH}]/[\text{Ti} + \text{Zr}]$  and  $[\text{CH}_3\text{COOH}]/[\text{Zr}]$  ratios exceeded 15 in our study. Doeuff et al. studied several titanium alkoxides and found that the product at  $[\text{CH}_3\text{COOH}]/[\text{Ti}] > 5$  was a water-soluble precipitate with stoichiometry  $\text{TiO}(\text{CH}_3\text{COO})_2$ .<sup>47</sup> The chemical composition of the product was the same in all cases, irrespective of the nature of the alkoxy group.

In an equimolar mixture of Zr *n*-propoxide and Ti-isopropoxide with acetic acid at  $[\text{CH}_3\text{COOH}]/[\text{Ti} + \text{Zr}] = 5$ , the resulting cluster was  $\text{Zr}_6\text{Ti}_3(\text{OPr})_{16}(\text{OAc})_8\text{O}_8$ , with Pr = iso- $\text{C}_3\text{H}_7$  or *n*- $\text{C}_3\text{H}_7$  and Ac = acetate.<sup>46</sup> Precipitation was observed when  $[\text{CH}_3\text{COOH}]/[\text{Ti} + \text{Zr}] > 5$ .

Acetic acid modification of pure Zr *n*-propoxide and *n*-butoxide showed that up to three acetate ligands can react with zirconium alkoxides.<sup>48</sup> Acetic acid is able to substitute terminal alkoxy groups without breaking the stable dimeric Zr–Zr unit present in these alkoxides.<sup>49</sup> Hence, the chemical structure of the oxoacetate clusters does not depend on the alkoxy group, but on the metallic center and alkoxide to acetic acid ratio. The actual structure of mixed zirconium/titanium oxoacetates should therefore depend on the  $[\text{Zr}]/[\text{Ti}]$  and  $[\text{CH}_3\text{COOH}]/[\text{Ti} + \text{Zr}]$  ratios. Our experiments show that zirconium oxoacetates are predominantly formed in solution, despite the high concentration of Ti precursor that was also present in solution. Since zirconium alkoxides are more susceptible to substitution or hydrolysis than titanium alkoxides,<sup>50</sup> this could explain why predominantly Zr-rich oxoacetates were formed in an excess of acetic acid. Titanium oxoacetates may also have formed, but due to their oligomeric character and the presence of other species in the system such as lead(II) acetate and zirconium-based oligomers, they remained amorphous. The zirconium oxoacetates formed in excess of acetic acid precipitated either in the sol ( $h < 5$ ) or in the drying thin film ( $h > 9$ ). Zirconium oxoacetate probably formed molecular crystals rather than disordered oligomers.<sup>45</sup> This would explain why the PZT precursor sols exhibited both crystalline Zr-rich regions and Ti-rich amorphous regions. Since zirconium oxoacetates are water-soluble, no or limited crystallization could take place at  $h > 100$ , when water was present in the film for a long time during the evaporation process. In the film drying process the zirconium oxoacetates could evolve into a crystalline  $\text{ZrO}_2$  phase. Such transitions typically require a relatively high temperature.<sup>24</sup> In the present case, however, we are dealing with a limited number of sub-10 nm particles. Possibly, the extensive drying in the electron microscope vacuum and the energy of the electron beam were sufficient to recrystallize zirconium oxoacetate into  $\text{ZrO}_2$ . In that case we cannot discriminate between the influence of the electron microscope measurement and spontaneous phase transformations induced by drying. Nevertheless, both the precursor sol and the as-dried thin films contain either zirconium oxoacetate or a crystalline  $\text{ZrO}_2$  nanophase.

#### 4. CONCLUSIONS

Zr-rich nanoparticles of 1–10 nm size are present in as-dried PZT films. At hydrolysis ratios up to at least 27.6, these

nanoparticles are crystalline, and the surrounding Ti- and Zr-rich matrix is amorphous. The crystalline nanoparticle phase originates from crystalline material that precipitates from a pure zirconia sol in an excess of acetic acid, and is most likely a nanocrystalline zirconium oxoacetate phase. At  $h < 5$ , the zirconium oxoacetate nanoparticle formed directly in fresh sols. Stable sols without a trace of crystallinity formed when  $h$  was between  $\sim 5$  and 27.6. But the same crystalline nanoparticle formed in situ when these sols were dried as thin films. At  $h > 100$ , no crystallization of Zr-rich nanoparticles occurred in either the sol or in the as-dried film.

Films prepared from aged sols had a higher degree of crystallinity than films from fresh sols. EELS maps of Ti and Zr indicate that their spatial distribution in an aged film fluctuated on a length scale of 80–100 nm. It seems that such compositional heterogeneity occurs on a longer length scale in films from aged sols than from fresh sols.

## ■ ASSOCIATED CONTENT

**S Supporting Information.** Electron energy loss spectra of Pb-M<sub>4,5</sub> from as-dried PZT thin film with  $h = 9.3$ . This material is available free of charge via the Internet at <http://pubs.acs.org>.

## ■ AUTHOR INFORMATION

### Corresponding Author

\*E-mail: [j.e.tenelshof@utwente.nl](mailto:j.e.tenelshof@utwente.nl).

## ■ ACKNOWLEDGMENT

This work was financially supported by The Netherlands Organization for Scientific Research (NWO) in the framework of the Innovational Research Incentive (VIDI Scheme). We thank NWO for providing us with beam time at the ESRF DUBBLE beamline. Dr. Giuseppe Portale and beamline staff of DUBBLE are thanked for their competent support.

## ■ REFERENCES

- (1) Scott, J. F.; Paz De Araujo, C. A. *Science* **1989**, *246*, 1400–1405.
- (2) Scott, J. F. *Science* **2007**, *315*, 954–959.
- (3) Murali, P. *J. Micromech. Microeng.* **2000**, *10*, 136–146.
- (4) Kondo, M.; Sato, K.; Ishii, M.; Wakiya, N.; Shinozaki, K.; Kurihara, K. *Jpn. J. Appl. Phys.* **2006**, *45*, 7516–7519.
- (5) Kim, H. R.; Jeong, S.; Jeon, C. B.; Kwon, O. S.; Hwang, C. S. *J. Mater. Res.* **2001**, *16*, 3583–3591.
- (6) Otani, Y.; Okamura, S.; Shiosaki, T. *J. Electroceram.* **2004**, *13*, 15–22.
- (7) Lin, Y. C.; Chuang, H. A.; Shen, J. H. *Vacuum* **2009**, *83*, 921–926.
- (8) Bouregba, R.; Poullain, G.; Vilquin, B.; Murray, H. *Mater. Res. Bull.* **2000**, *35*, 1381–1390.
- (9) Zhu, T. J.; Lu, L.; Lai, M. O. *Appl. Phys. A: Mater. Sci. Process.* **2005**, *81*, 701–714.
- (10) Dekkers, M.; Nguyen, M. D.; Steenwelle, R.; te Riele, P. M.; Blank, D. H. A.; Rijnders, G. *Appl. Phys. Lett.* **2009**, *95*, 0129021–0129023.
- (11) Schwartz, R. W. *Chem. Mater.* **1997**, *9*, 2325–2340.
- (12) Schwartz, R. W.; Boyle, T. J.; Lockwood, S. J.; Sinclair, M. B.; Dimos, D.; Buchheit, C. *Integr. Ferroelectr.* **1995**, *7*, 259–277.
- (13) Yi, G.; Sayer, M. *Ceram. Bull.* **1991**, *70*, 1173–1179.
- (14) Klee, M.; Eusemann, R.; Waser, R.; Brand, W.; van Hal, H. *J. Appl. Phys.* **1992**, *72*, 1566–1576.
- (15) Cui, T.; Markus, D.; Zurn, S.; Polla, D. L. *Microsyst. Technol.* **2004**, *10*, 137–141.
- (16) Schwartz, R. W.; Voigt, J. A.; Tuttle, B. A.; Payne, D. A.; Reichert, T. L.; DaSalla, R. S. *J. Mater. Res.* **1997**, *12*, 444–456.
- (17) Assink, R. A.; Schwartz, R. W. *Chem. Mater.* **1993**, *5*, 511–517.
- (18) Zhang, M.; Salvado, I. M. M.; Vilarinho, P. M.; Silvestre, A. J. D.; Silva, A. M. S. *J. Am. Ceram. Soc.* **2007**, *90*, 358–363.
- (19) Caruso, R.; de Sanctis, O.; Frattini, A.; Gil, C. S. R. *Surf. Coat. Technol.* **1999**, *122*, 44–50.
- (20) Boyle, T. J.; Dimos, D.; Schwartz, R. W.; Alam, T. M.; Sinclair, M. B.; Buchheit, C. D. *J. Mater. Res.* **1997**, *12*, 1022–1030.
- (21) Zhang, Q.; Huang, Z.; Vickers, M. E.; Whatmore, R. W. *J. Eur. Ceram. Soc.* **1999**, *19*, 1417–1421.
- (22) Zhang, Q.; Vickers, M. E.; Patel, A.; Whatmore, R. W. *J. Sol–Gel Sci. Technol.* **1998**, *11*, 141–152.
- (23) Zhang, Q.; Whatmore, R. W.; Vickers, M. E. *J. Sol–Gel Sci. Technol.* **1999**, *15*, 13–22.
- (24) Schwartz, R. W.; Schneller, T. S.; Waser, R. C. R. *Chim.* **2004**, *7*, 433–461.
- (25) Schwartz, R. W.; Narayanan, M. *Chemical Solution Deposition—Basic Principles*. In *Solution Processing of Inorganic Materials*; Mitzi, D. B., Ed.; John Wiley & Sons: Hoboken, NJ, USA, 2009; pp 33–76.
- (26) Malic, B.; Kosec, M.; Arcon, I.; Kodre, A. *J. Eur. Ceram. Soc.* **2005**, *25*, 2241–2246.
- (27) Chae, H. K.; Payne, D. A.; Xu, Z.; Ma, L. *Chem. Mater.* **1994**, *6*, 875–877.
- (28) Brethon, A.; Hubert-Pfalzgraf, L. G. *J. Sol–Gel Sci. Technol.* **2006**, *39*, 159–167.
- (29) Brethon, A.; Hubert-Pfalzgraf, L. G.; Daran, J. C. *Dalton Trans.* **2006**, 250–257.
- (30) Hubert-Pfalzgraf, L. G.; Daniele, S.; Papiernik, R.; Massiani, M. C.; Septe, B.; Vaissermann, J.; Daran, J.-C. *J. Mater. Chem.* **1997**, *7*, 753–762.
- (31) Daniele, S.; Papiernik, R.; Hubert-Pfalzgraf, L. G.; Jagner, S.; Hikansson, M. *Inorg. Chem.* **1995**, *34*, 628–632.
- (32) Brinker, C. J.; Hurd, A. J.; Schunk, P. R.; Frye, G. C.; Ashley, C. S. *J. Non-Cryst. Solids* **1992**, *147–148*, 424–436.
- (33) Wilkinson, A. P.; Xu, J.; Pattanaik, S.; Billinge, S. J. L. *Chem. Mater.* **1998**, *10*, 3611–3619.
- (34) Khan, S. U.; Göbel, O. F.; Blank, D. H. A.; ten Elshof, J. E. *Appl. Mater. Interfaces* **2009**, *10*, 2250–2255.
- (35) Rasband, W. S. *ImageJ*; U.S. National Institute of Health: Bethesda, MD, USA, 1997–2011 (<http://imagej.nih.gov/ij/>).
- (36) Bras, W.; Dolbnya, I. P.; Detollenaere, D.; van Tol, R.; Malfois, M.; Greaves, G. N.; Ryan, A. J.; Heeley, E. J. *Appl. Crystallogr.* **2003**, *36*, 791–794.
- (37) Craievich, A. F. *Mater. Res.* **2002**, *5*, 1–11.
- (38) Glatter, O.; Kratky, O. *Small Angle X-ray Scattering*; Academic Press: London, 1982; pp 17–52.
- (39) Lamas, D. G.; Rosso, A. M.; Suarez-Anzorena, M.; Fernandez, A.; Bellino, M. G.; Cabezas, M. D.; Walsöe de Reaca, N. E.; Craievich, A. F. *Scr. Mater.* **2006**, *55*, 553–556.
- (40) Bhagwat, M.; Ramaswamy, V. *Mater. Res. Bull.* **2004**, *39*, 1627–1640.
- (41) Piszczek, A.; Radtke, A.; Grodzicki, A.; Wojtczak, A.; Chojnacki, J. *Polyhedron* **2007**, *26*, 679–685.
- (42) Kogler, F. R.; Jupa, M.; Puchberger, M.; Schubert, U. *J. Mater. Chem.* **2004**, *14*, 3133–3138.
- (43) Puchberger, M.; Kogler, F. R.; Jupa, M.; Gross, S.; Fric, H.; Kicelbick, G.; Schubert, U. *Eur. J. Inorg. Chem.* **2006**, *16*, 3283–3293.
- (44) Malic, B.; Arcon, I.; Kodre, A.; Kosec, M. *J. Sol–Gel Sci. Technol.* **1999**, *16*, 135–141.
- (45) Sengupta, S. S.; Ma, L.; Adler, D. L.; Payne, D. A. *J. Mater. Res.* **1995**, *10*, 1345–1348.
- (46) Laaziz, I.; Larbot, A.; Julbe, A.; Guizard, C.; Cot, L. *J. Solid State Chem.* **1992**, *98*, 393–403.
- (47) Doeuff, S.; Henry, M.; Sanchez, C. *Mater. Res. Bull.* **1990**, *25*, 1519–1529.
- (48) Peter, D.; Erstel, T. S.; Bertagnolli, H. *J. Sol–Gel Sci. Technol.* **1995**, *5*, 5–14.
- (49) Peter, D.; Erstel, T. S.; Bertagnolli, H. *J. Sol–Gel Sci. Technol.* **1994**, *3*, 91–99.
- (50) Wright, J. D.; Sommerdijk, N. A. J. M. *Sol–Gel Materials Chemistry and Applications. Advanced Chemistry Texts*; CRC Press: Boca Raton, FL, 2001; pp 53–68.